

## Double Diffusion, Shear Instabilities, and Heat Impacts of a Pacific Summer Water Intrusion in the Beaufort Sea

ELIZABETH C. FINE,<sup>a,b</sup> JENNIFER A. MACKINNON,<sup>b</sup> MATTHEW H. ALFORD,<sup>b</sup> LEO MIDDLETON,<sup>c</sup> JOHN TAYLOR,<sup>c</sup> JOHN B. MICKETT,<sup>d</sup> SYLVIA T. COLE,<sup>a</sup> NICOLE COUTO,<sup>b</sup> ARNAUD LE BOYER,<sup>b</sup> AND THOMAS PEACOCK<sup>e</sup>

<sup>a</sup> Woods Hole Oceanographic Institution, Woods Hole, Massachusetts

<sup>b</sup> Scripps Institution of Oceanography, University of California, San Diego, La Jolla, California

<sup>c</sup> University of Cambridge, Cambridge, England

<sup>d</sup> Applied Physics Laboratory, University of Washington, Seattle, Washington

<sup>e</sup> Massachusetts Institute of Technology, Cambridge, Massachusetts

(Manuscript received 26 March 2021, in final form 22 November 2021)

**ABSTRACT:** Pacific Summer Water eddies and intrusions transport heat and salt from boundary regions into the western Arctic basin. Here we examine concurrent effects of lateral stirring and vertical mixing using microstructure data collected within a Pacific Summer Water intrusion with a length scale of  $\sim 20$  km. This intrusion was characterized by complex thermohaline structure in which warm Pacific Summer Water interleaved in alternating layers of  $\mathcal{O}(1)$  m thickness with cooler water, due to lateral stirring and intrusive processes. Along interfaces between warm/salty and cold/freshwater masses, the density ratio was favorable to double-diffusive processes. The rate of dissipation of turbulent kinetic energy ( $\varepsilon$ ) was elevated along the interleaving surfaces, with values up to  $3 \times 10^{-8} \text{ W kg}^{-1}$  compared to background  $\varepsilon$  of less than  $10^{-9} \text{ W kg}^{-1}$ . Based on the distribution of  $\varepsilon$  as a function of density ratio  $R_\rho$ , we conclude that double-diffusive convection is largely responsible for the elevated  $\varepsilon$  observed over the survey. The lateral processes that created the layered thermohaline structure resulted in vertical thermohaline gradients susceptible to double-diffusive convection, resulting in upward vertical heat fluxes. Bulk vertical heat fluxes above the intrusion are estimated in the range of  $0.2\text{--}1 \text{ W m}^{-2}$ , with the localized flux above the uppermost warm layer elevated to  $2\text{--}10 \text{ W m}^{-2}$ . Lateral fluxes are much larger, estimated between  $1000$  and  $5000 \text{ W m}^{-2}$ , and set an overall decay rate for the intrusion of  $1\text{--}5$  years.


**KEYWORDS:** Arctic; Diapycnal mixing; Diffusion; Fluxes; Instability; Mixing; Turbulence

### 1. Introduction

In the western Arctic, Pacific-origin water acts as a heat reservoir in the upper ocean. Pacific Water enters the Chukchi Sea via the Bering Strait at an annual mean rate of approximately  $1 \text{ Sv}$  ( $1 \text{ Sv} \equiv 10^6 \text{ m}^3 \text{ s}^{-1}$ ) (Woodgate 2018). During the summer and early autumn, insolation in the shallow Chukchi Sea and Alaskan river outflow further warms and freshens this water mass (Timmermans et al. 2018). This relatively warm water subducts as it enters the Arctic Basin, where it contributes to the upper halocline layer of the Canada Basin, forming Pacific Summer Water (PSW), generally characterized by salinity between 30 and 33 (Timmermans et al. 2014). Pacific Summer Water can be further classified into warmer and fresher Alaskan Coastal Water, which forms off the Alaskan coast during the summer with input from Alaskan rivers, and cooler summer Bering Sea Water, which takes a more circuitous path through the Chukchi Sea. These warm water masses lie higher in the water column than the colder and saltier Pacific Winter Water, which forms from Pacific-origin water in shelf seas during the winter and enters the Arctic Basin along similar pathways.

From 1987 to 2017, the heat content within a salinity range of 31–33 nearly doubled (Timmermans et al. 2018). There are spatial correlations between newly ice-free regions in the summer and areas of increased temperature in the warm halocline, suggesting PSW heat may contribute to the loss of Arctic sea ice (Stroeve and Notz 2018). However, the pathways by which PSW influences sea ice are not well understood. Mixing rates in the stratified western Arctic are generally quite low, and shallow mixed layers with strong haloclines inhibit vertical heat fluxes from deeper water masses to the surface (Fer 2009; Toole et al. 2010; Jackson et al. 2010; Lincoln et al. 2016). Thus upward heat flux from the PSW layer is likely low except during rare events in which conditions conspire to overcome these barriers to diapycnal mixing. Therefore, understanding such events is key to unraveling the relationship between warming PSW and sea ice decline in the Beaufort Sea.

Previous observations have captured significant episodic upward heat fluxes out of anomalously warm PSW intrusions into the Canada Basin. These include warm anticyclonic eddies (Kawaguchi et al. 2012; Fine et al. 2018) and less coherent filaments or intrusions (Kawaguchi et al. 2014; Timmermans and Jayne 2016; MacKinnon et al. 2021). In these events, upward heat fluxes of  $\mathcal{O}(1\text{--}10) \text{ W m}^{-2}$  have been inferred, demonstrating the importance of near-surface features in the transport of Pacific-origin heat into the mixed layer. However, as subsurface PSW intrusions are often transient and have weak surface expression, identifying them and assessing their lifetime and subsequent impact on vertical heat fluxes is a challenge.

 Denotes content that is immediately available upon publication as open access.

Corresponding author: Effie Fine, efine@whoi.edu

DOI: 10.1175/JPO-D-21-0074.1

© 2022 American Meteorological Society. For information regarding reuse of this content and general copyright information, consult the AMS Copyright Policy (www.ametsoc.org/PUBSReuseLicenses).

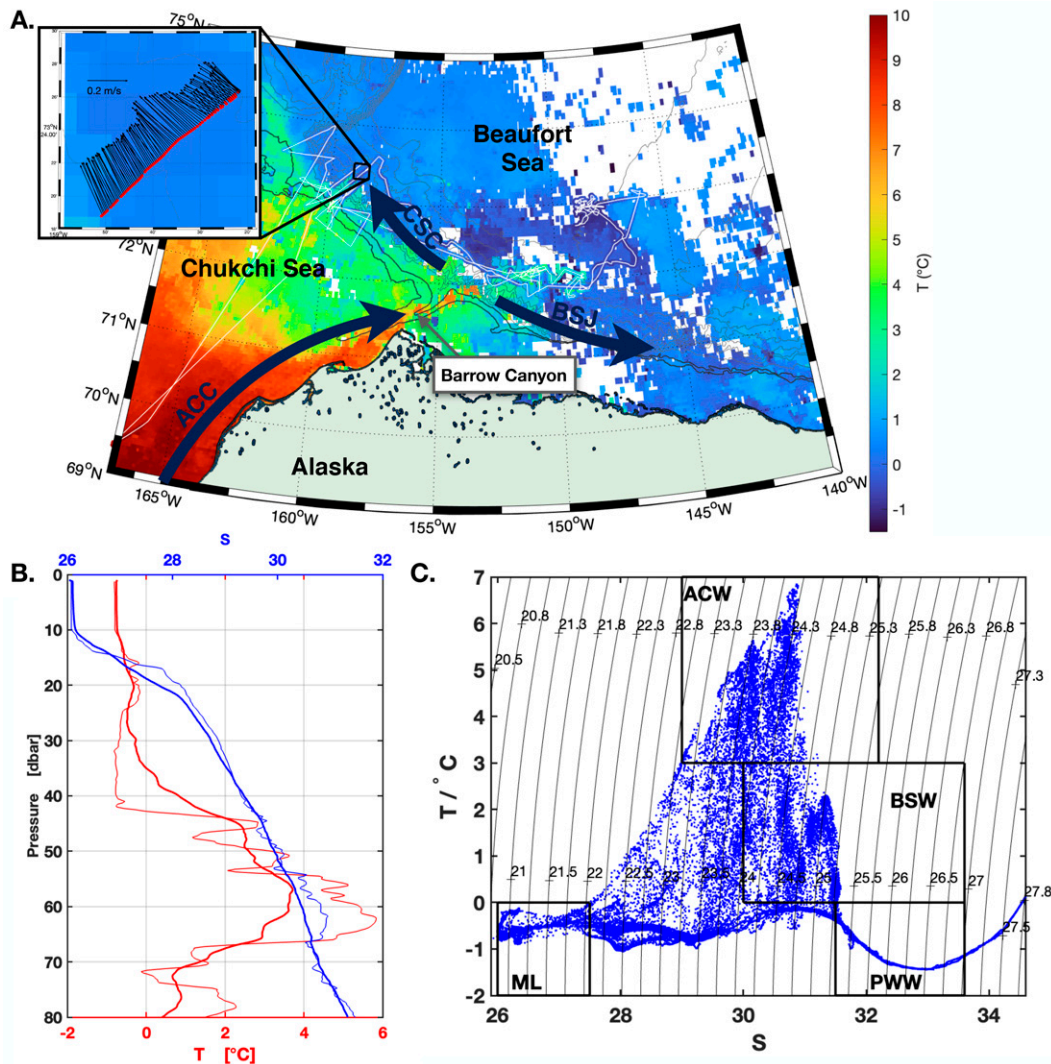


FIG. 1. (a) Map of the survey region with cruise track shown in white. Color shows monthly SST from MODIS-Aqua for September 2018 (Werdell et al. 2013), except along cruise track where it is colored by SST as observed from the ship. Inset highlights the 2018 Chukchi Slope Current survey, with mean velocity vectors from 15- to 80-m depth. Schematic currents are shown for the Alaskan Coastal Current (ACC), Chukchi Slope Current (CSC), and Beaufort Shelfbreak Jet (BSJ). (b) Mean temperature and salinity profile over the CSC intrusion survey (thick), with a single profile to demonstrate  $T$ - $S$  structure (thin). (c)  $T$ - $S$  diagram for the intrusion survey.

In the current study, we examine a PSW intrusion in order to address these key questions. This intrusion was embedded in the Chukchi Slope Current (CSC), which carries water from the Barrow Canyon outflow to the northwest with typical velocities in the range of  $10 \text{ cm s}^{-1}$  (Fig. 1; Corlett and Pickart 2017). In the summer months this current represents a pathway for Alaskan Coastal Water (Corlett and Pickart 2017; Boury et al. 2020). Microstructure observations capture the PSW intrusion actively undergoing both lateral stirring and vertical mixing. These observations provide an opportunity to determine the dominant mixing processes that mediate vertical heat fluxes that may directly affect sea ice as well as the lateral fluxes that control how such intrusions eventually mix into the surrounding waters.

In warm intrusions, both double diffusion and shear-driven turbulence can drive diapycnal and isopycnal heat flux (Fine et al. 2018; Kawaguchi et al. 2014; Ruddick et al. 2010; Merrifield et al. 2016). To investigate the role of these two processes, we begin by considering the distribution of turbulent dissipation rate  $\varepsilon$  as a function of Richardson number (a measure of shear) and the density ratio (a measure of susceptibility to double diffusive processes). We compare these distributions to illuminate the relative importance of shear versus double diffusion to determining  $\varepsilon$  over the survey.

In the next phase of analysis, we examine two different methods of estimating  $\varepsilon$  from finescale observations, which we use as an alternate approach to determining the relative roles of shear

and double diffusion in setting turbulent dissipation rates. Recently Middleton et al. (2021) described a method to estimate the dissipation rate due to double diffusion from along-isopycnal spice variance based on the theory described in Middleton and Taylor (2020). This method generally reproduced the microstructure dissipation rates reported in Fine et al. (2018), except in a region where shear instability was thought to explain elevated dissipation rates. In the current study we apply the method from Middleton et al. (2021) to estimate the contribution of double diffusion to total  $\varepsilon$ . We compare the results of this method to a shear-based internal wave parameterization Gregg (1989), which we use to assess where shear instabilities may drive turbulence. We find that a superposition of these two models qualitatively reproduces the main features of observed  $\varepsilon$ .

Finally, we estimate vertical and lateral heat fluxes and an intrusion decay time scale. We find that lateral processes determine the time scale for the intrusion's decay, consistent with observations of other warm and salty intrusions (Ruddick et al. 2010; Fine et al. 2018).

In section 2 we describe the data used in this study, and in section 3 we describe methods of analysis. Section 4 presents results from the intrusion survey, an investigation of the relative roles of double diffusion and shear-driven mixing, and estimates of intrusion heat fluxes. In section 5 we provide a summary of results thus far. In section 6 we conclude with a brief discussion of the significance of the intrusion's heat transport.

## 2. Data

Observational data were collected from the R/V *Sikuliaq* during the September 2018 Office of Naval Research (ONR)-funded Stratified Ocean Dynamics of the Arctic (SODA) process cruise. Microstructure measurements were taken using the Modular Microstructure Profiler (MMP). The MMP is a loosely tethered free-falling turbulence profiler developed by M. C. Gregg at the Applied Physics Laboratory of the University of Washington. The MMP falls at nominally  $0.6 \text{ m s}^{-1}$ , and carries two custom-built shear probes, an FP07 thermistor, a pumped SeaBird CTD, and an altimeter. The SeaBird CTD consists of an SBE-3 model ocean thermometer and an SBE-4 model conductivity sensor, with a sample rate of 25 Hz. The shear probes and FP07 thermistor both sample at 400 Hz. The MMP has a maximum profiling depth of 300 m. In this survey profiles were only taken to 100 m to maximize horizontal resolution.

The present paper focuses on a warm intrusion observed on 26 September 2018 during a transect perpendicular to the Chukchi slope (Fig. 1a, inset). The survey was conducted at  $73.37^\circ\text{N}$ ,  $158.63^\circ\text{W}$  and consisted of 74 MMP profiles taken over 6.5 h, corresponding to a spatial resolution of approximately 400 m.

## 3. Methods

The TKE dissipation rate [ $\varepsilon = (15/2)\nu\overline{(\partial u/\partial z)^2}$ , in which  $\nu$  is the kinematic viscosity] is calculated from microstructure shear measurements by iteratively fitting a Panchev curve to

shear spectra calculated over 2.5-s (1–2-m) windows [indicated by the overbar of  $(\partial u/\partial z)^2$ ] (Alford and Gregg 2001). The noise floor for  $\varepsilon$  is  $10^{-10} \text{ W kg}^{-1}$ . Gridded data products were created by binning both CTD data and microstructure data to 0.25-m bins. Salinity is reported as practical salinity (unitless) and temperature as in situ temperature ( $^\circ\text{C}$ ) for consistency with prior measurements with the microstructure system.

The fast response thermistor from the MMP can generally be used to calculate the dissipation rate of thermal variance,  $\chi = 6\kappa_T\langle T_z^2 \rangle$ , in which  $\kappa_T$  is the molecular diffusivity of heat and  $\langle T_z^2 \rangle$  is the variance of the vertical thermal gradient. However, in the current survey small-scale variance in temperature was induced both by the turbulent motions traditionally associated with  $\chi$  and by thermohaline interleaving, resulting in small-scale temperature variance not associated with turbulence. The difficulty of separating turbulent and intrusive scales results in significant (2–3 orders of magnitude) overestimates of diffusivity and related fluxes if  $\chi$  is calculated using standard spectral methods and then used to infer turbulent mixing rates [see, e.g., the appendix of Fine et al. (2018)]. Thus, for the analysis that follows we have only used  $\varepsilon$  to identify turbulence and calculate bulk diffusivities. The exception is in a small region in which diffusive convective steps could be identified by eye from the FP07 temperature data. Within this region, both  $\chi$  and  $\varepsilon$  were calculated in hand-selected windows that span convecting layers, avoiding the jumps in temperature across interfaces, as described in Fine et al. (2018).

Velocity data were collected using a 300-kHz ADCP and binned to 2 m in depth. Shear is calculated as the first difference of velocity in depth, and is taken over 2 m except where otherwise specified.

The gradient Richardson number  $\text{Ri} = N_{6m}^2/|U_{z6m}|^2$  can be used to infer the prevalence of shear instabilities. We filter density data using a 4-m Bartlett filter to match the ADCP response characteristics, then interpolate CTD and velocity data onto the same 2-m grid. All quantities are then smoothed over 0.5 km in the horizontal (corresponding to approximately two MMP profiles) to compare the data. Both  $N^2$  and  $U_z$  are calculated from 6-m first differences. Density is sorted to enforce gravitational stability prior to calculating  $N^2$  (as well as true overturning, mismatches in the response time of the temperature and conductivity sensors can result in erroneous overturns). The 6-m first-differencing scale is chosen to eliminate high wavenumber noise in shear. Generally shear instabilities may occur where  $\text{Ri} < 0.25$  (Miles 1961; Howard 1961). However, this method cannot detect shear instabilities on scales smaller than 6 m, and is thus likely biased high.

The potential for double diffusive convection can be assessed using the density ratio, defined here as

$$R_\rho = \frac{\beta\Delta S}{\alpha\Delta T} \quad (1)$$

in which  $\alpha$  and  $\beta$  are the thermal expansion and haline contraction coefficients



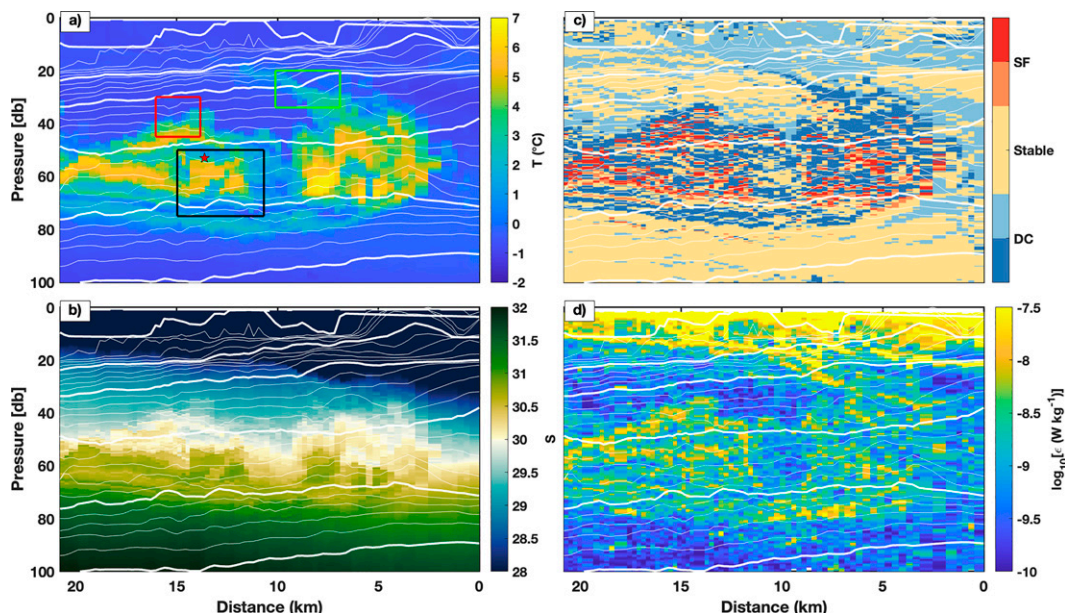


FIG. 2. (a) Temperature ( $^{\circ}\text{C}$ ), (b) salinity ( $\text{g kg}^{-1}$ ), (c) double-diffusive stability based on  $R_{\rho}$  (see section 3), and (d)  $\log_{10}(\epsilon)$  ( $\text{W kg}^{-1}$ ) measured during the CSC intrusion microstructure survey. The  $x$  axis represents distance along the cruise track and is inverted so that the right edge of the plot represents the western end of the survey line (the transect was sampled traveling east to west). Isopycnals are shown in white at intervals of  $0.2 \text{ kg m}^{-3}$ , with heavier lines every  $1 \text{ kg m}^{-3}$  labeled on the left of (a). The temperature and salinity color scales in (a) and (b) are both oversaturated to emphasize contrast within the intrusion layer. In (c), colors map to  $R_{\rho}$  as follows: red corresponds to the salt fingering regime, with bright red for  $1/2 < R_{\rho} < 1$  and light red for  $0 < R_{\rho} < 1/2$ ; blue corresponds to the diffusive convective regime, with bright blue for  $1 < R_{\rho} < 10$  and light blue for  $R_{\rho} > 10$ ; yellow corresponds to  $R_{\rho} < 0$ , representing either doubly stable stratification or gravitational instability. Colored boxes in (a) indicate subsections of the survey in which microstructure temperature is reproduced in Fig. 3.

$$\alpha = -\frac{1}{\rho} \frac{\partial \rho}{\partial T} \bigg|_{S,p} \quad \text{and} \quad \beta = -\frac{1}{\rho} \frac{\partial \rho}{\partial S} \bigg|_{T,p}, \quad (2)$$

and  $\Delta S/\Delta T$  is the ratio of the vertical gradient of salinity to the vertical gradient of temperature (Fig. 2c). In this analysis gradients are calculated by first-differencing adjacent 0.25-m depth bins and smoothed in the vertical by 2 m. Double diffusion may occur where  $R_{\rho} > 0$ , that is, where both temperature and salinity either increase or decrease in depth ( $R_{\rho} < 0$  indicates either double diffusive stability or gravitational instability). Where  $R_{\rho} > 1$ , the water column is susceptible to diffusive layering, while when  $0 < R_{\rho} < 1$  salt fingering may occur. In general, coherent staircases of diffusive layering are only found where  $1 < R_{\rho} < 10$ , while salt fingering staircases occur where  $1/2 < R_{\rho} < 1$  (Kelley et al. 2003).

Variations in temperature and salinity contribute to variations in density according to the thermal and haline expansion coefficients  $\alpha$  and  $\beta$ . Assuming a linear equation of state, the quantity  $\text{spice}$  is defined along isopycnals as  $s_p \equiv \alpha T + \beta S$ , so that “spicier” conditions are warmer and saltier at a given density (Veronis 1972; Klein et al. 1998; Smith and Ferrari 2009).

A number of methods have been developed to infer  $\epsilon$  where microstructure measurements are not available, depending on the turbulent processes leading to mixing.

Throughout much of the ocean, internal waves play a dominant role in setting mixing rates. Finescale parameterizations have been used to estimate mixing due to the downscale transfer of energy in the internal wavefield, with remarkable success in the global ocean (Whalen et al. 2015). Limited opportunistic studies in the western Arctic suggest these parameterizations may be equally effective in this environment (Guthrie et al. 2013; Fine et al. 2021). Polzin et al. (2014) provides a full description of the basis for these parameterizations. Kawaguchi et al. (2016) compared the semiempirical parameterization developed by Gregg (1989) with microstructure measurements in the Chukchi Plateau, finding relatively good agreement. Following this method we estimate  $\epsilon$  due to internal waves as

$$\epsilon_{G89} = \epsilon_0 \frac{N_{6m}^2}{N_0^2} \frac{S_{6m}^4}{S_{GM}^4}. \quad (3)$$

Here,  $\epsilon_0 = 7 \times 10^{-10} \text{ W kg}^{-1}$  is the Garrett–Munk rate of dissipation of TKE,  $N_{6m}$  and  $S_{6m}$  are the buoyancy frequency and shear calculated over 6-m differences, respectively;  $N_0 = 5.2 \times 10^{-3} \text{ rad s}^{-1}$  is the Garrett–Munk buoyancy frequency; and  $S_{GM}$  is the Garrett–Munk shear.

We additionally estimate the double-diffusive contribution to  $\epsilon$  following recent work by Middleton et al. (2021). In this

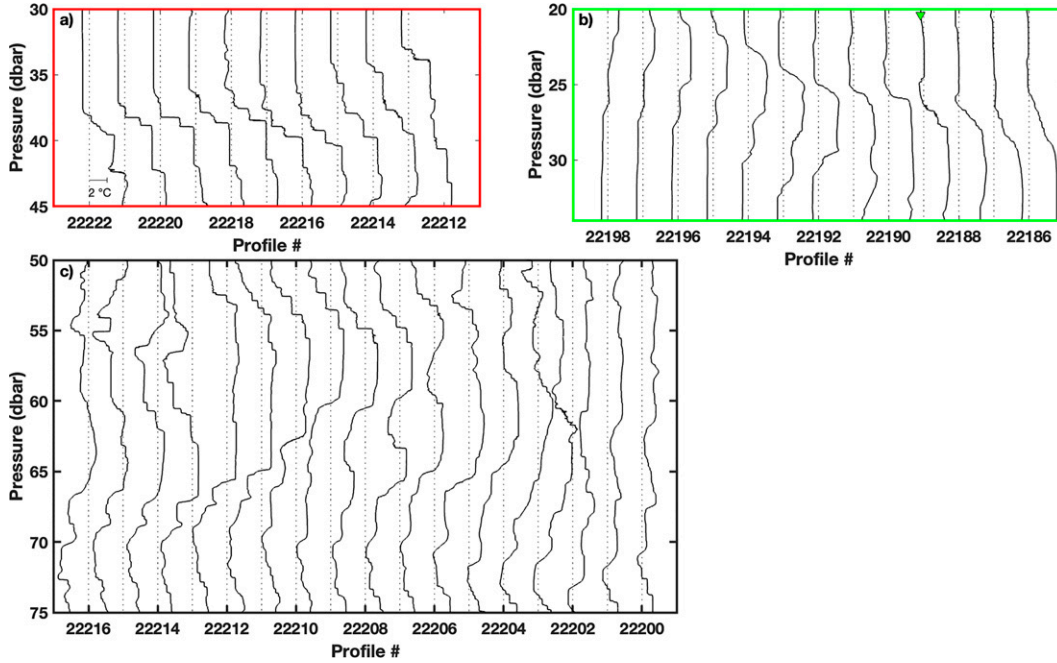


FIG. 3. High-resolution temperature profiles from the FP07 sensor over three representative subsets of the survey. Colors outlining each panel correspond to the colored boxes in Fig. 2a. These subsets show (a) a region with visible diffusive-convective layering, (b) a region with relatively high shear, in which a green triangle above profile 22189 denotes a profile with spikes in temperature that may be indicative of active shear-driven mixing, and (c) a region with pronounced lateral intrusions, which exist across all vertical scales. In all panels, the x axis is inverted, so that the right edge of the panel represents the western edge of the survey. The temperature scale is denoted by a horizontal line in profile 22222, in (a).

method, the local along-isopycnal spice variance from a  $T$ - $S$  section is extrapolated to the scale of 3D turbulence using a model spectrum. The double-diffusive dissipation rate is then linked to the upgradient diapycnal buoyancy flux using the theory outlined in Middleton and Taylor (2020). A brief description of the assumptions this method requires and the steps to apply it is provided in the appendix. In this method,  $\varepsilon$  is estimated as

$$\langle \varepsilon \rangle = -\frac{\kappa_T + \kappa_S}{2b_z^*} \langle |\nabla b|^2 \rangle + g \frac{\kappa_T - \kappa_S}{2b_z^*} \langle |\nabla b| \rangle \sqrt{\frac{2}{3} + \frac{N^2}{3f^2}} \sqrt{\frac{A}{2}} k_{Oz} \quad (4)$$

in which  $\kappa_T$  and  $\kappa_S$  are the molecular diffusivities of heat and salt, respectively;  $b$  is buoyancy;  $b_z^*$  is the gradient of the sorted buoyancy profile;  $g$  is acceleration due to gravity;  $N$  is the buoyancy frequency;  $f$  is the Coriolis frequency;  $A$  is the magnitude of the spice gradient; and  $k_{Oz}$  is the wavenumber associated with the Ozmidov length scale. Quantities are calculated as the implicit average between observations. This equation is solved iteratively, as described in the appendix.

## 4. Results

### a. Intrusion hydrographic and dynamic structure

The warm intrusion contained water with temperatures up to  $7^\circ\text{C}$  and salinities of approximately 30.5 (Figs. 2a,b), consistent with the  $T$ - $S$  properties of Alaskan Coastal

Water (Timmermans et al. 2014). While the survey location was near relatively warm SST along the Chukchi shelf, the temperatures observed in the intrusion were significantly warmer than either surface or interior temperatures observed in the Chukchi Sea during the course of the process cruise, and were similar instead to outflows from Barrow Canyon and other warm intrusions embedded in the Chukchi Slope Current (Fig. 1; see also Boury et al. 2020; MacKinnon et al. 2021).

Temperature and salinity profiles within the intrusion revealed complex fine structure. Interleaving layers of relatively warm and salty water alternated with layers that were cold and fresh. These layers were most apparent in the FP07 temperature (Fig. 3c), and occur over a wide range of scales. To a large degree the  $T$ - $S$  structure was density compensated, with warm and salty coherent structures crossing isopycnals (Figs. 2a,b). This compensation is visually apparent along the top and bottom of the warm intrusion in Fig. 2a, in which the curvature of the warm signal often opposes the isopycnal curvature in white. Density-compensated lateral fronts in temperature and salinity can lead to vertical layering due to double diffusion, as described by Ruddick and Turner (1979), among others. Ruddick and Turner (1979) introduced a scaling for the height of double-diffusive thermohaline intrusions as a function of  $T$ - $S$  properties,

$$H = \frac{3}{2} (0.44) \frac{\beta \Delta S}{\frac{1}{\rho} \frac{d\rho}{dz}} \quad (5)$$

in which  $\beta$  is the haline contraction coefficient and  $\Delta S$  is the salinity difference across a lateral front. Taking  $\beta$ ,  $\rho$ , and  $dp/dz$  as the survey-averaged values between 0- and 80-m depth, considering a range of  $\Delta S$  from 0.1 to 0.5 (consistent with the isopycnal variation in salinity over the survey) results in a range of thermohaline layers from 1 to 5 m. This height scale is consistent with the observations, although the instrument cannot realistically resolve salinity at scales smaller than 1 m (Fig. 2c). Thus, we hypothesize that the observed layering was initially induced by double-diffusive thermohaline intrusions that occurred along a lateral front. Isopycnal stirring of these layers could create the observed smaller-scale temperature structure (Bebieva and Timmermans 2019).

In general, double diffusive layers of this nature slope relative to isopycnals, with the direction of the intrusion slope relative to the isopycnal slope corresponding to the dominance of diffusive convective or salt fingering forms of double diffusion (May and Kelley 2001). In this survey the curvature of isotherms relative to isopycnals varies both laterally and with depth, with isotherms sloping upward/downward along the first half of the section above/below the intrusion, and in the opposite sense over the second half. The observed varying isotherm slope relative to isopycnals may be the result of differential advection with depth applied to the layered structure (Smith and Ferrari 2009).

In  $T$ - $S$  space, three distinct water masses can be identified: cold and fresh surface water associated with the mixed layer, the intrusion of warm PSW, and colder, saltier Pacific Winter Water (PWW). A primary temperature peak appears at 7°C and a salinity of 30, consistent with Alaskan Coastal Water (ACW) with a slightly fresher peak at 5.5°C (Fig. 4). A second cooler and saltier peak occurs at 2°C and a salinity of 31, and is likely associated with summer Bering Seawater. Much of the  $T$ - $S$  space between the warmest Alaskan Coastal Water, the cold surface, and cold Pacific Winter Water is represented within the survey, suggesting that both isopycnal and diapycnal mixing between these endpoints is ongoing, as discussed in the next section.

The intrusion was embedded within the CSC (Fig. 1a). Data collected during the survey show strong cross-track (northwestern) surface intensified velocity, consistent with other CSC observations (Fig. 1a, inset, and Figs. 5a,b) (Corlett and Pickart 2017; Boury et al. 2020). A small-scale (~7 km) velocity feature was associated with the  $T$ - $S$  anomalies of the intrusion, in which vertical shear was intensified in a layer from 10 to 30 m beneath the surface (Figs. 5c,d). Beneath 20 m, the northwest flow was somewhat relaxed. However, the velocity increased around 70 m with a corresponding deeper shear layer. Geostrophic cross-track shear is qualitatively similar to measured cross track shear but smaller, implying an ageostrophic component to this small feature (Fig. 5e). Assuming a CSC speed of 0.2 m s<sup>-1</sup>, it would have taken the intrusion about 9 days to travel from the mouth of Barrow Canyon (where it likely originated) to the survey location.

Spice variation can be used to characterize length scales and processes of lateral stirring (Cole and Rudnick 2012; Timmermans et al. 2012; Timmermans and Winsor 2013). Lateral spectra

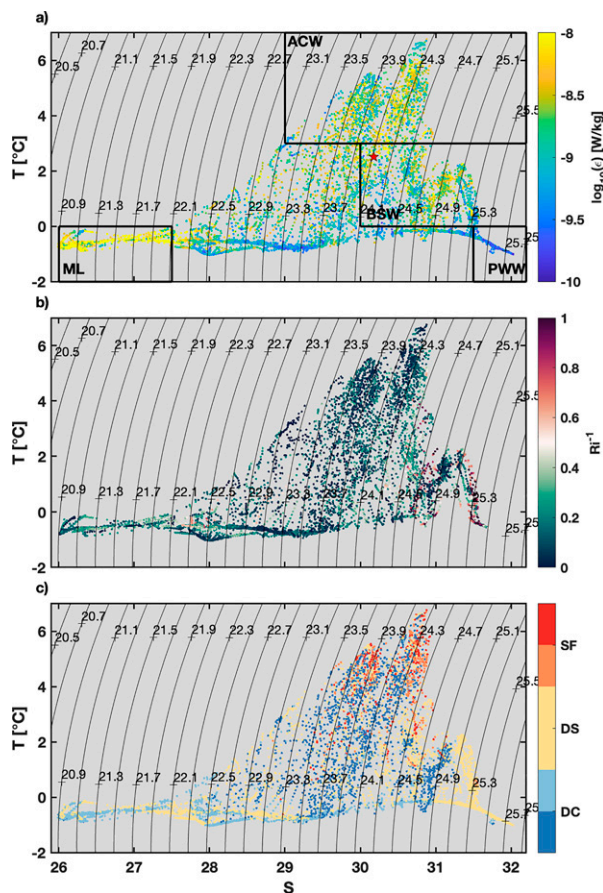


FIG. 4. Temperature (°C) and salinity colored by (a)  $\log_{10}(\epsilon)$  ( $W\ kg^{-1}$ ), (b)  $Ri^{-1}$ , and (c) double-diffusive stability based on  $R_p$  (see section 3; colors are as in Fig. 2).

of  $\alpha T$ ,  $\beta S$ , and  $s_p$  along isopycnals show spice variations are dominated by temperature, with  $\alpha T$  about 10 times larger than  $\beta S$  over the considered wavenumber range, indicating that temperature is close to a passive tracer (Fig. 6). The spice spectra approximate a  $k^{-2}$  spectral slope over scales from 500 m to 10 km. While few observations consider spectra at these small horizontal scales, this slope is consistent with glider observations in the North Pacific by Cole and Rudnick (2012), who found isopycnal salinity spectral slopes of  $k^{-2}$  at scales of 15–100 km. This is a steeper slope than the  $k^{-1}$  slope associated with quasigeostrophic turbulence, which Middleton et al. (2021) applied in the Arctic eddy described by Fine et al. (2018). This difference in steepness suggests that the small-scale eddies which control isopycnal stirring are of different predominance in the two surveys. The current intrusion was observed in a more active environment due to the influence of the Chukchi Slope Current, so it is perhaps unsurprising that the details of lateral stirring are different in this environment.

Both the  $T$ - $S$  properties and the velocities associated with the CSC intrusion indicate an active environment in which both shear and double diffusive instabilities may occur, while along-isopycnal variations in spice indicate the presence of



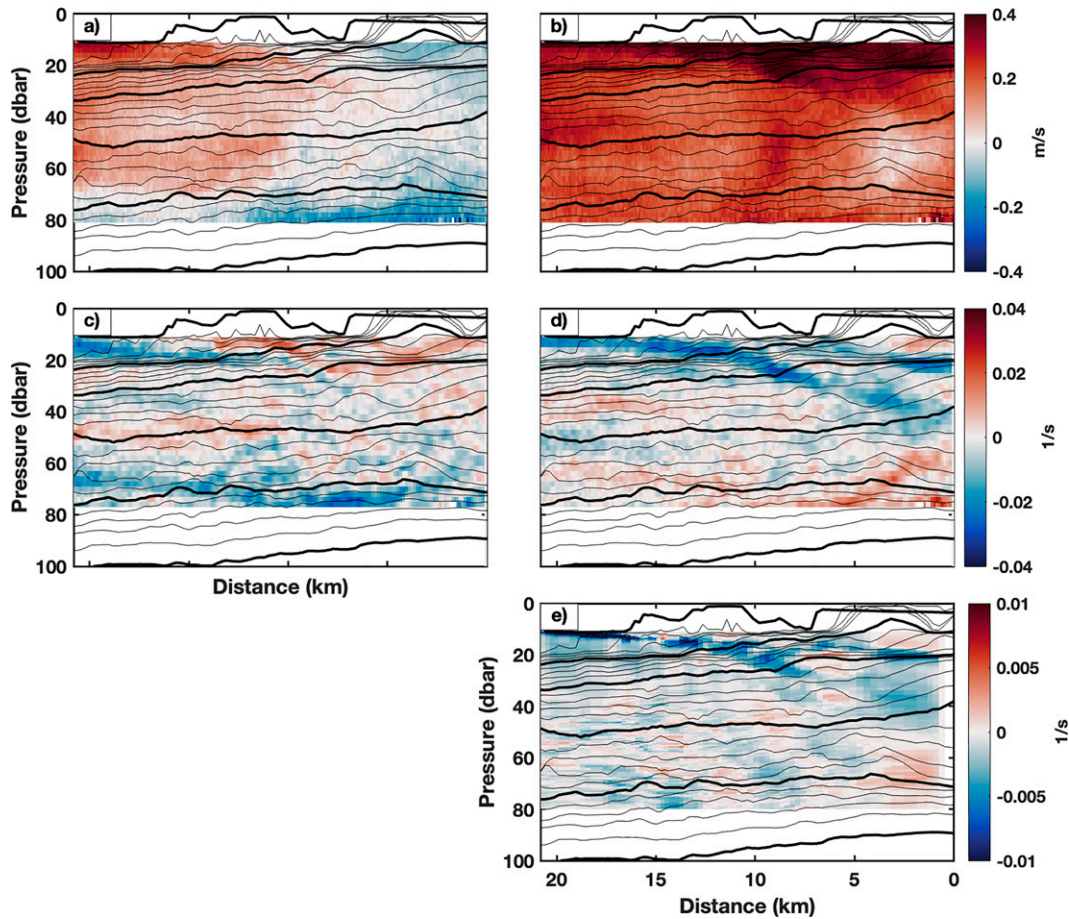


FIG. 5. Measured velocity from the shipboard ADCP during the CSC intrusion survey (a) along and (b) across the ship track; measured shear from the shipboard ADCP during the CSC intrusion survey (c) along and (d) across the ship track; (e) cross-track geostrophic shear calculated from MMP survey. Isopycnals are shown in black (at the same intervals as in Fig. 2).

lateral stirring. In the next section we consider microstructure observations of  $\varepsilon$ , the relationships between  $Ri$ ,  $R_\rho$ , and  $\varepsilon$ , and methods to infer  $\varepsilon$  in the absence of microstructure data, with the aim of understanding the processes responsible for the evolution of the CSC intrusion.

#### b. Turbulence observations and models

Total vertical shear  $|\mathbf{U}_z|^2 = U_z^2 + V_z^2$  was elevated above and below the intrusion due to the presence of the CSC (Fig. 7a). The buoyancy frequency  $N^2$  showed structure similar to shear (Fig. 7b). Relatively low  $Ri$  (high  $Ri^{-1}$ ) highlights potential areas of shear instability along the top and bottom edges of the intrusion (Fig. 7c). Some high-resolution temperature profiles in which  $Ri$  is low show variation typical of turbulent mixing (Fig. 3b, particularly profile 22189). As  $Ri$  is calculated over 6-m scales it is a relatively coarse measurement, and is never less than 1. In the analysis that follows, we use  $Ri = 3$  as a cutoff for “low”  $Ri$ , chosen so that the relatively low  $Ri$  values just above the warm peak are included. The color scale in Fig. 7c is set so that the white point indicates this cutoff.

The complex thermohaline structure provided favorable conditions for double-diffusive instabilities. Throughout the intrusion,  $R_\rho$  has layered small-scale structure, with regions strongly favorable to salt fingering and diffusive convection alternating on scales as small as 1 m (Fig. 2). Conditions favorable to diffusive convection ( $R_\rho > 1$ ) and salt fingering ( $0 < R_\rho < 1$ ) occur above and below local temperature maxima, respectively. The small-scale layering in  $R_\rho$  demonstrates that the vertical gradients in temperature and salinity associated with the largely density-compensated structure of the intrusion may have implications for diapycnal heat fluxes within the intrusion. Indeed, examination of temperature profiles above and below temperature maxima show evidence of diffusive layers associated with diffusive convection and salt fingering, respectively (Fig. 3c). Above temperature maxima (e.g., 53–55 m) profiles show a distinct staircase pattern, with thin (10 cm) interfaces over which temperature changes rapidly separating convecting layers, which are frequently less than a meter thick. Below warm intrusions (e.g., profiles 22212 and 22213 around 66 m) salt fingering appears as steps which cool with depth, although the layers and interfaces are

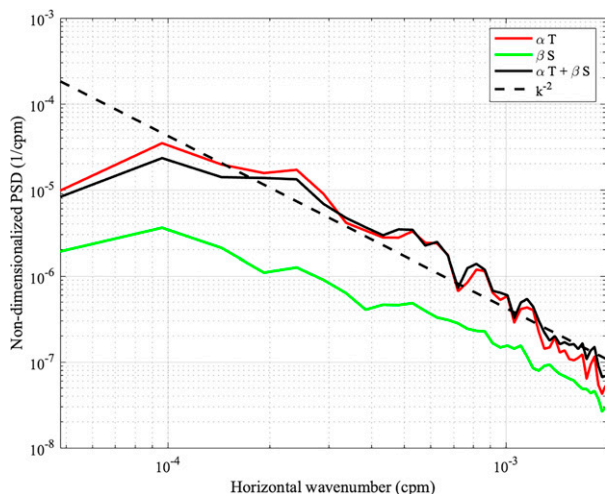


FIG. 6. Spectra in isopycnal coordinates of salinity, temperature, and spice (see text for definition). Spectra are averaged over the isopycnal range from  $\sigma_\theta = 22.4 \text{ kg m}^{-3}$  to  $\sigma_\theta = 25.1 \text{ kg m}^{-3}$ .

less distinct in the salt fingering case. Intermittent spikes in the temperature profile, visible in profiles 22203, 22207, and 22209 may indicate local shear instability.

Consistent with these indications of instability, turbulent kinetic energy dissipation ( $\varepsilon$ ) was elevated within, above, and below the intrusion. The small-scale variations in  $\varepsilon$  reflect the intricate  $T$ - $S$  structure within the intrusion, with elevated  $\varepsilon$  coinciding with regions in the diffusive convection and salt-fingering regimes (Fig. 2d). The area of high inverse

Richardson number around 20 m deep at 7 km is also characterized by high  $\varepsilon$  (Fig. 7d).

Considering  $\varepsilon$  in  $T$ - $S$  space emphasizes that turbulent dissipation rates are relatively high in the water column directly above  $T$ - $S$  peaks, implying upward heat flux (Fig. 4a). The inverse Richardson number is rarely greater than one in these areas, with most areas of potential instability above and below the  $2^\circ\text{C}$  isotherm that bounds the intrusion (Figs. 4b and 7c). Conditions favorable to diffusive convection are common where  $\varepsilon$  is high, suggesting that diffusive convection contributes to elevated  $\varepsilon$  on the upper edge of warm/salty layers due to the motion of convecting cells. Salt-fingering favorable conditions are associated with lower levels of  $\varepsilon$  (Figs. 4a,c). Dissipation rates are generally low where the water column is double-diffusively stable, except at salinity less than 28 where mixed layer dynamics are present.

### 1) RELATIVE INFLUENCE OF SHEAR INSTABILITY AND DOUBLE DIFFUSION

Observed  $R_p$  (Fig. 2c),  $Ri$  (Fig. 7c), and  $\varepsilon$  (Figs. 2d and 7d) indicate that both low  $Ri$  and double-diffusively favorable  $R_p$  were associated with elevated  $\varepsilon$ . In this section we examine the relative roles of each process by binning  $\varepsilon$  based on stability criteria.

High  $\varepsilon$  values where  $Ri^{-1}$  is high (Figs. 7c,d) suggest shear instability plays a role in generating mixing. We bin  $\varepsilon$  values based on  $Ri$ , defining  $Ri < (\geq) 3$  as “small” (“large”)  $Ri$ , and calculate probability density functions (PDFs) and histograms based on  $\log_{10}(\varepsilon)$  for all measurement bins between 15 and 75 m. A higher cutoff for  $Ri$  than the commonly used  $Ri = 1$

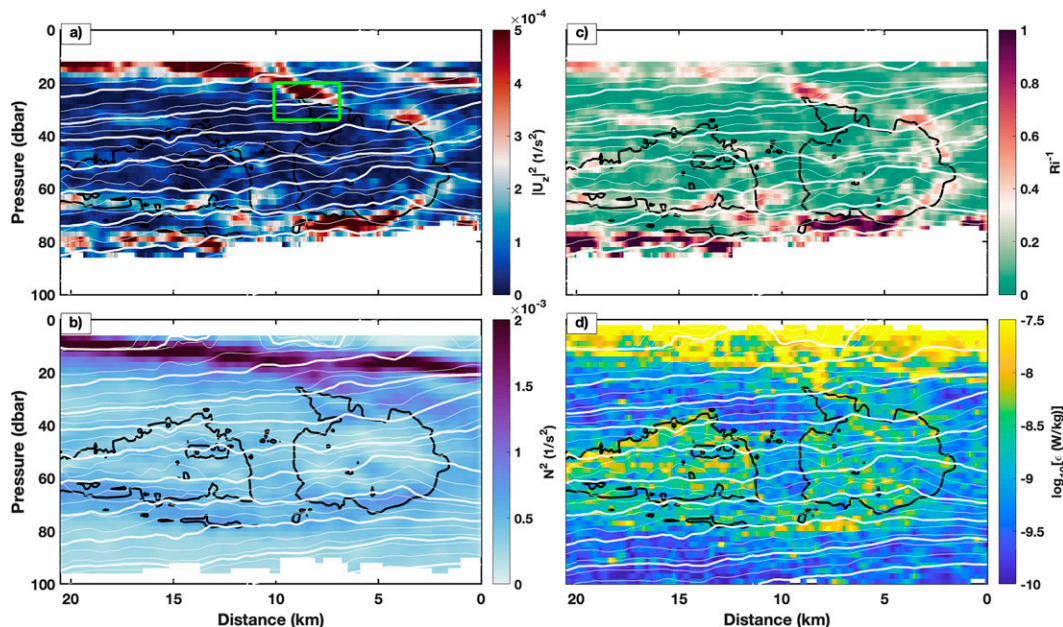


FIG. 7. (a)  $|U_z|^2$ , (b)  $N^2$ , (c)  $Ri^{-1}$ , (d)  $\log_{10}(\varepsilon)$  measured during the CSC intrusion survey, all interpolated onto the same grid as the ADCP velocity and smoothed over 4 m in the vertical and 0.5 km in the horizontal. Isopycnals are shown in white in (a); all other panels show the smoothed  $2^\circ\text{C}$  isotherm.



was used so that the cluster of low Ri values identified around the deeper warm peak (Fig. 4b) were included within the cut-off. As expected, slightly higher  $\varepsilon$  values are associated with small values of Ri (Fig. 8a), but these conditions were rare throughout the survey, with large Ri bins accounting for a large majority of measurements (5421 bins = 94% of measurements; Fig. 8d). A Kolmogorov–Smirnov test indicates that the differences between the distributions for large and small Ri were statistically significant at the 95% confidence level.

The two distinct types of double-diffusive convection, diffusive convection (DC) and salt fingering (SF), also are both associated with elevated  $\varepsilon$  (Figs. 2c,d and 4a,c). Double-diffusive convection results in elevated  $\varepsilon$  as energy is dissipated by the motion of convecting cells. Binning  $\log_{10}(\varepsilon)$  values based on double-diffusive stability criteria (i.e., Fig. 2c) indicates that doubly stable conditions and weak DC are both associated with lower  $\varepsilon$ , while strong DC is associated with higher  $\varepsilon$  (Fig. 8b). Both weak and strong SF are associated with intermediate  $\varepsilon$ . DC bins are the most common (2875 bins = 49%), while SF is relatively rare (483 bins = 8%, Fig. 8e). Only the differences between strong and weak DC are statistically significant at the 95% confidence level.

To compare the influence of shear and double diffusion, we interpolate temperature and salinity onto the same grid as velocity. Following St. Laurent and Schmitt (1999) and Merrifield et al. (2016), we bin  $\varepsilon$  values by both Ri and double-diffusive stability between 15 and 65 m (below 65 m, Ri is suspect due to noise in shear). For this analysis, strong and weak SF and DC are all treated as double-diffusive susceptible. Considering the resulting four PDFs, some patterns emerge (Fig. 8c). Bins in which observations indicate stability to both double diffusion and shear are associated with the lowest values of  $\varepsilon$  ( $\langle \varepsilon \rangle = 1.0 \times 10^{-9} \text{ W kg}^{-1}$ ). Bins that are stable to double diffusion but potentially susceptible to shear instabilities have only slightly higher mean  $\varepsilon$  values ( $\langle \varepsilon \rangle = 1.3 \times 10^{-9} \text{ W kg}^{-1}$ ). Double-diffusive susceptible bins are associated with higher values of  $\varepsilon$  ( $\langle \varepsilon \rangle = 1.5 \times 10^{-9} \text{ W kg}^{-1}$ ), with bins susceptible to both double diffusion and shear instabilities having the highest mean ( $\langle \varepsilon \rangle = 2.2 \times 10^{-9} \text{ W kg}^{-1}$ ). The general influence of shear on double diffusion is an area of ongoing research beyond the scope of the current work (see, e.g., Padman 1994; Shibley and Timmermans 2019; Brown and Radko 2019). However, these results suggest that in these observations, shear enhances dissipation due to double diffusion. The differences between all four distributions are statistically significant at 95% confidence intervals according to a Kolmogorov–Smirnov test.

A small secondary peak is apparent in bins that are double-diffusively stable but susceptible to shear instabilities at  $\varepsilon = 10^{-7} \text{ W kg}^{-1}$ . These bins are associated with the isolated burst of shear-driven turbulence around 20 m deep.

A stacked histogram emphasizes the dominant role of double diffusion in setting dissipation rates (Fig. 8f). The vast majority of bins (5244 = 91%) have large Ri, but many (3335 = 61%) are favorable to double diffusion, particularly at higher values of  $\varepsilon$ . Thus, while high shear is likely responsible for some of the highest values of  $\varepsilon$ , these events are so rare (even in this relatively

high-shear environment) that double diffusion is the dominant factor.

Considering where the highest values of  $\varepsilon$  occur provides another way to interpret these results. Of the upper 10th percentile values of  $\varepsilon$ , the proportion which have  $\text{Ri} < 3$  or  $R_\rho > 0$  is given in Table 1. Only 16% of these bins have  $\text{Ri} < 3$ , while 75% have  $R_\rho > 0$ . The 20% of upper 10th percentile  $\varepsilon$  bins with double diffusively stable stratification and high Ri emphasize the limitations of this analysis. Elevated  $\varepsilon$  in these bins may (i) result from instabilities on scales smaller than the resolution of our ADCP and/or conductivity sensor, (ii) persist after mixing has resulted in a doubly stable profile or large-scale shear has dissipated, or (iii) be linked with horizontal shear production (Baker and Gibson 1987). The current analysis is insufficient to determine the cause of elevated  $\varepsilon$  in all instances.

While this analysis suggests that DC is the dominant cause of elevated  $\varepsilon$ , it is possible that the thermohaline gradients that define the contours of the intrusion are subject to strong shear due to the lateral stirring of the intrusion. Thermohaline layers exist on scales that are too small to be resolved by the ADCP observations and, without higher resolution shear measurements, it is impossible to eliminate this hypothesis.

Due to the strong double-diffusive instabilities identified along these thermohaline gradients and the separation in PDFs based on the type of double-diffusive instability, we suspect that double diffusion plays a substantial role in setting dissipation rates. Whether DC or finescale shear ultimately sets the rates of turbulence, the result is elevated  $\varepsilon$  along high thermal gradients, resulting in a net transport of heat out of the warm intrusion (consistent with the patterns observed in Fig. 4).

## 2) MIXING MODELS AND PARAMETERIZATIONS

As microstructure measurements require specialized instruments and sampling there is a strong motive to develop methods to estimate mixing rates solely from more readily available temperature, salinity, and velocity data. These efforts become complicated when multiple processes set turbulent mixing rates in a given region. The results of the previous analysis suggest that both shear and double diffusion play distinct roles in setting turbulent dissipation rates over this survey. Here we compare the results of a finescale parameterization for shear-driven turbulence due to internal waves with a novel method to infer dissipation rates due to double diffusion. We also compare the sum of these two parameterizations with observed  $\varepsilon$  and discuss the extent to which each of these approaches reproduces observed spatial patterns.

Finescale parameterizations infer diapycnal mixing rates based on shear and strain of the internal wavefield. Following Gregg (1989), we estimate  $\varepsilon$  due to internal waves from observed 6-m shear and buoyancy frequency (see section 3). The resulting estimate  $\varepsilon_{\text{G89}}$  bears some resemblances to observed  $\varepsilon$  ( $\varepsilon_{\text{obs}}$ ), particularly above and below the intrusion where shear and  $\varepsilon_{\text{G89}}$  are elevated (Fig. 9a). However,  $\varepsilon_{\text{G89}}$  is

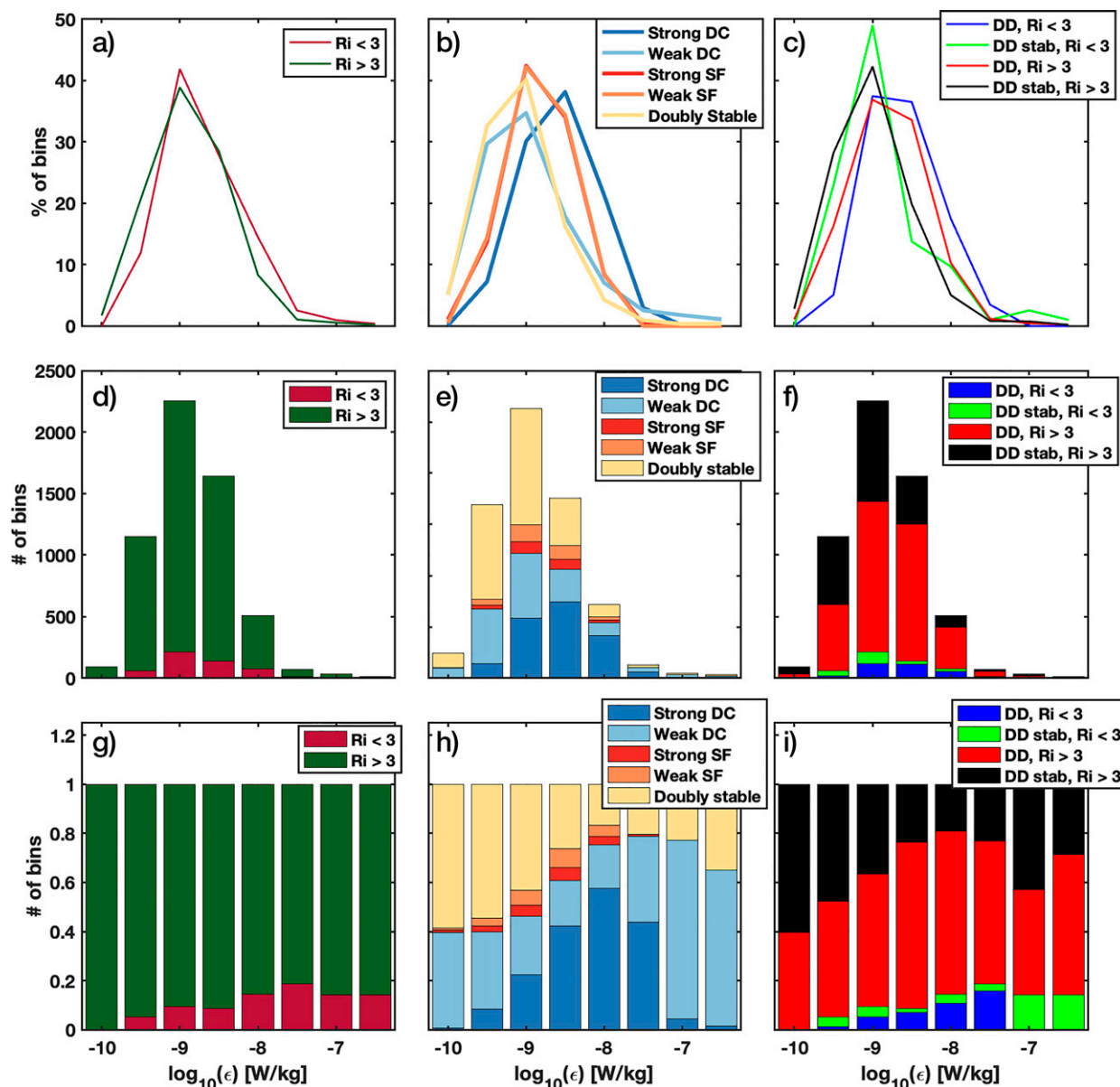


FIG. 8. (a)–(c) PDFs, (d)–(f) stacked histograms, and (g)–(i) histograms normalized by total observations in each  $\epsilon$  bin of  $\log_{10}(\epsilon)$  binned by (left)  $Ri$ , (center) double-diffusive stability, and (right) both  $Ri$  and double-diffusive stability.

biased low throughout the survey, and particularly in the interior of the intrusion (Figs. 9f,g). This is unsurprising as fine-scale parameterizations do not account for double diffusive processes and thus underestimate double diffusive mixing rates (Gregg 1989; Polzin et al. 2014).

TABLE 1. Percent of bins with upper 10th percentile values of  $\epsilon$  subject to double-diffusive and shear instability criteria.

	Double diffusive	Doubly stable	Total
$Ri < 3$	11%	5%	16%
$Ri > 3$	64%	20%	84%
Total	75%	25%	

In recent work, Middleton et al. (2021) described a method to estimate the double-diffusive contribution to  $\epsilon$  from isopycnal spice variance (see section 3). High isopycnal spice variance is associated with differential spice advection, which results in vertical double diffusive instabilities of both DC and SF types. To our knowledge this is the only existing model that infers double diffusive  $\epsilon$  based on energetic constraints without assuming the type of double diffusive convection. In the observations discussed above, we inferred that lateral processes (including small-scale double-diffusive lateral intrusions and isopycnal stirring) set the stage for both DC and SF mixing mechanisms, suggesting that the assumptions of Middleton et al.'s (2021) method are appropriate for the current study. A key assumption of this

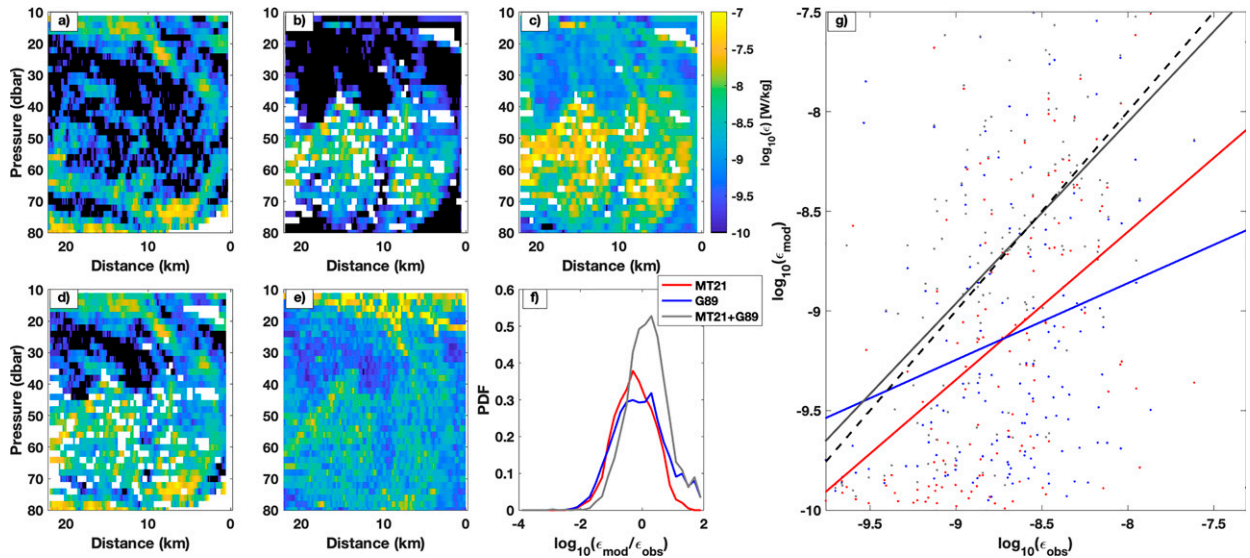


FIG. 9. Estimates of  $\epsilon$  from (a) Gregg (1989) finescale parameterization, (b) Middleton et al. (2021) spice model assuming a subgrid-scale spectral slope of spice of  $k^{-2}$ , (c) Middleton et al. (2021) spice model assuming a subgrid-scale spectral slope of spice of  $k^{-1}$ , (d) estimated  $\epsilon$  obtained by adding the results of (a) and (b), and (e) microstructure observations. Comparisons of the models with data are shown as (f) histograms of the ratio of modeled and observed  $\epsilon$  and (g) comparison of results of each method with observed  $\epsilon$ , after gridding to a lower resolution grid with 4-m vertical resolution and 2-km horizontal resolution. Lines of best fit to the data are shown, with a black dashed line indicating a one-to-one line. In (a)–(e), black color indicates bins in which  $\epsilon$  estimates were below the  $10^{-10}$   $\text{W kg}^{-1}$  noise floor of the MMP, which are excluded from analysis in (f) and (g). The Middleton et al. (2021) spice model is based on an iterative method; bins in which this method fails to converge are in white.

method is that the rate at which temperature variance is stirred along isopycnals controls the rate of double diffusion, and thus the rate of dissipation. As we cannot measure isopycnal temperature variance at all scales, the method uses an assumed spectral slope for the horizontal wavenumber spectra to infer the rate of lateral stirring. Extrapolating from the isopycnal spice variance calculated over our dataset (Fig. 6), we assume a  $k^{-2}$  spectral slope of spice at subgrid scales. Applying this method to the MMP CTD data results in an estimate  $\epsilon_{\text{MT21}}$  that is elevated within the intrusion and effectively reproduces much of the structure in observed  $\epsilon$  (Fig. 9b). The  $k^{-2}$  slope assumed here based on the observed spice spectra is steeper than the  $k^{-1}$  slope assumed in Middleton et al. (2021) over a prior warm eddy survey. The predicted  $\epsilon$  generated from this model using a  $k^{-1}$  slope is biased high relative to observations (Fig. 9c). The steeper slope necessary to produce  $\epsilon_{\text{MT21}}$  estimates that match observations in the current study compared to the results described by Middleton et al. (2021) suggest that the scales of lateral stirring are not consistent across the two surveys.

As the two  $\epsilon$  models each show qualitative success in different regions of the intrusion, we consider the quantity  $\epsilon_{\text{MT21}} + \epsilon_{\text{G89}}$  by adding the results of the Gregg (1989) and Middleton et al. (2021) applied with a  $k^{-2}$  slope (Fig. 9d). The interaction between shear and double diffusion is more complicated than this simple approach implies; however, due to the lognormal distribution of  $\epsilon$  the additive product of the two models emphasizes the high values that are relevant for mixing in each model. The superposition performs better than either model alone, and qualitatively captures the main features of  $\epsilon_{\text{obs}}$  (Figs. 9f,g); 86% of the results from the superimposed model are within an order

of magnitude of observed values, and 46% are within a factor of 2.

### c. Heat fluxes and decay scales

The CSC intrusion contained anomalously warm water, thus even molecular diffusivities would result in the loss of heat from the interior of the intrusion to the surrounding water due to downgradient heat fluxes. Elevated  $\epsilon$  over the intrusion and the presence of diffusive convective layers suggests that these losses are significantly larger than molecular diffusivity would suggest (Figs. 2 and 3). The complex structure of temperature results in a vertical gradient, and corresponding heat fluxes, that change sign rapidly with depth. In this section we quantify instantaneous vertical fluxes over a small section of the upper edge of the intrusion, and the decay time scale associated with these fluxes.

#### 1) VERTICAL HEAT FLUX

The layered structure of the intrusion results in vertical heat fluxes that alternate direction. The dominance of diffusive convection in setting higher values of  $\epsilon$  may indicate a net upward flux as the upper edge of each warm layer is most turbulent; however, quantifying this net effect is complicated by the interleaving structures at small scales. Along the uppermost edge of the intrusion quantifying vertical heat flux is more tractable. Here, discrete diffusive convective layers can be seen in microstructure data (Fig. 3b).



To calculate heat fluxes, convecting layers in which temperature was approximately constant were selected by hand over the profiles and depth range shown in Fig. 3. This subset of the data was chosen as this was where the convective layered structure was clearest. Forty-four layers were identified this way, with a mean layer height of 1.5 m (standard deviation 0.9 m) and a mean  $R_\rho$  of 1.5 (standard deviation 0.3). Within each layer, two methods were used to estimate the vertical temperature diffusivity within the layer. The Osborn–Cox relation

$$K_T = \frac{\chi}{2T_z^2} \quad (6)$$

is used to estimate the thermal diffusivity from  $\chi$  measurements, while the Osborn relation

$$K_\rho \leq \Gamma \varepsilon / N^2, \quad (7)$$

is used to estimate thermal diffusivity from  $\varepsilon$  measurements, taking the mixing efficiency  $\Gamma = 1$  as this is applied only within the convective layers. Heat flux from each method is calculated as  $F_H = \rho C_p K_T T_z$ , and is calculated locally within every layer. This method is identical to that used to calculate the heat flux due to diffusive layers in Fine et al. (2018). The mean vertical heat flux over the 44 identified layers is  $19 \text{ W m}^{-2}$  using the Osborn–Cox method (from  $\chi$ ) and  $14 \text{ W m}^{-2}$  from the Osborn method. As the measurement uncertainty for both  $\chi$  and  $\varepsilon$  is a factor of 2–3, this qualifies as good agreement between methods.

We additionally estimated heat flux across the staircases using the flux law for diffusive convection described by Kelley (1990):

$$F_{4/3} = 0.0032 \exp\left(\frac{4.8}{R_\rho^{0.72}}\right) \rho C_p \left(\frac{\alpha g \kappa}{P_r}\right)^{1/3} \delta \theta^{4/3}, \quad (8)$$

in which  $P_r = \nu/\kappa$  is the dimensionless Prandtl number and  $\delta\theta$  is the potential temperature difference across each layer. The estimate from the 4/3 flux law was  $71 \text{ W m}^{-2}$ , more than a factor of 3 larger than the microstructure measurements.

A final estimate of vertical heat flux was made from the molecular heat flux across the thin interfaces between the diffusive convective layers. We identified 21 such interfaces (not all convecting steps are separated by a single clear interface) with a mean interface height of 10 cm (standard deviation 4 cm). We calculated the heat flux across each of them as

$$F_{\text{mol}} = \rho C_p \kappa_T T_z \quad (9)$$

in which  $\kappa_T$  is the molecular diffusivity of heat, and  $T_z$  is calculated over the interface. Mean  $F_{\text{mol}}$  across all interfaces was  $7 \text{ W m}^{-2}$ .

There are some uncertainties associated with each of these methods. Layers and interfaces are selected by hand, and the average temperature gradient over convective layers is small ( $0.2^\circ \text{ C m}^{-1}$ ) so that the results are sensitive to the judgment of the researcher selecting layers, as well as the time response of the thermistor. However, the estimates from  $\chi$ ,  $\varepsilon$ , and the molecular heat flux agree within a factor of 3. Interfaces in

low  $R_\rho$  staircases may exhibit thermal diffusivity slightly higher than molecular rates due to the strength of convection (e.g., Sommer et al. 2014), which could explain why  $F_{\text{mol}}$  is lower than the estimates from microstructure measurements. In a direct comparison to microstructure observations, Umlauf et al. (2018) found that while the 4/3 flux parameterization largely agreed well with microstructure-inferred fluxes it tended to overestimate heat fluxes within the range  $1.3 < R_\rho < 1.8$ . The  $R_\rho$  in the current measurements falls within this range, which may lead to overestimation of fluxes from this method. Finally, it is possible that the Osborn–Cox method systemically overestimates the heat flux, as some of the microscale temperature variability may be due to lateral effects rather than purely 1D vertical mixing (Davis 1994). This discrepancy is consistent with the calculations by Alford et al. (2005), in which  $K_T$  calculated via the Osborn–Cox equation was higher than  $K_T$  calculated from the Osborn equation in a region with thermohaline intrusions, which was attributed to the influence of lateral stirring of thermal variance on  $\chi$ .

As the microstructure estimates of heat flux agree well with each other (in spite of their differing dependence on layer  $T_z$ ) and incorporate all available data, we proceed by taking their average and estimating the vertical heat flux within this region as  $16 \text{ W m}^{-2}$ .

## 2) DECAY TIME SCALES

We can estimate a characteristic decay time scale associated with the double diffusive heat flux by modeling the temperature evolution as  $dT/dt = F_T/(\rho c_p H_T)$ , in which  $H_T$  is the thickness of the temperature anomaly. The vertical heat flux due to double diffusion along the uppermost edge of the intrusion is transient, as the warm layers are thin and will lose their heat rapidly. Assuming a thickness of  $\sim 10 \text{ m}$  and a temperature difference of  $\sim 4^\circ \text{ C}$  from the base of the diffusive staircase to its top, these vertical fluxes are associated with a time scale of 3–6 months.

This time scale is likely much faster than the decay time scale for the entire intrusion. Once the gradients homogenize enough to suppress double diffusion, there likely to be very little background dissipation, as evidenced by the low values of  $\varepsilon$  observed outside of the intrusion. Thus the intrusion itself may persist long past the complex thermohaline layering.

## 5. Discussion and conclusions

This study provides a novel view of a warm Alaskan Coastal Water intrusion embedded in the Chukchi slope current and in the process of actively mixing into surrounding Arctic waters. At the point of observation, lateral processes had created a complex double-diffusive susceptible thermohaline structure. The intrusion was characterized by complex thermohaline layering, with layers at scales less than 1 m. Turbulent dissipation rates were elevated along strong thermohaline gradients in the intrusion, enhancing net transport of heat from the warm intrusion into the surrounding water. The temperature and salinity characteristics of the intrusion are consistent with Alaskan Coastal Water. As the intrusion was found along a known pathway for Barrow Canyon

outflow (Corlett and Pickart 2017), we suggest that it originated at Barrow Canyon and advected with the Chukchi slope current, taking approximately 9 days to arrive at the survey location. MacKinnon et al. (2021) observed the process by which similarly warm water subducted north of Barrow Canyon that same September.

Observations show elevated dissipation rates both where the thermohaline structure is double-diffusively susceptible and where Richardson number is relatively low. Statistical analysis indicates that the highest values of  $\varepsilon$  are associated with low Richardson number, but that double-diffusive convection occurred more frequently and is thus the dominant cause of the elevated dissipation over the survey.

Two models to reproduce  $\varepsilon$  observations from CTD and velocity data were examined. The Gregg (1989) finescale parameterization tended to underestimate dissipation rates in the intrusion interior where double diffusion likely contributed to elevated turbulence the most, but qualitatively reproduced the elevated  $\varepsilon$  observed above and below the intrusion, where shear was higher. Middleton et al.'s (2021) method, which estimates  $\varepsilon$  due to double diffusion, underestimated  $\varepsilon$  in the high shear regions, but reproduced the elevated  $\varepsilon$  observed in the intrusion's interior. A superposition of the two methods qualitatively reproduced  $\varepsilon$  observations remarkably well.

The strikingly high estimates of vertical heat fluxes in this intrusion are driven by double diffusion that results due to the complex thermohaline structure. High vertical heat fluxes due to double diffusion above warm PSW intrusions have also been observed by Kawaguchi et al. (2012) and Fine et al. (2018), and analogous observations in the Baltic Sea also found double diffusive heat fluxes of  $\mathcal{O}(10)$  W m<sup>-2</sup> Umlauf et al. (2018). Other observations of Pacific Summer Water intrusions do not generally have this degree of complex structure (Kawaguchi et al. 2012; Timmermans and Jayne 2016; Fine et al. 2018), suggesting that the thermohaline layering may be destroyed on relatively fast time scales, consistent with our estimate of 3–6 months for decay of the fine structure. Once the internal structure homogenizes, the associated mixing rates would likely drop to very low background mixing rates. The mean temperature between 40 and 80 m depth over the survey is 2.3°C, so that even without any lateral flux outside of the intrusion homogenization within the survey would result in significantly weaker thermal gradients than those observed.

### Basin significance

The CSC intrusion carried significant subsurface heat that was actively mixing into the surrounding waters. These observations demonstrate a pathway by which heat can be transported from the basin boundaries into the interior. The along-track heat density of the intrusion relative to the freezing point  $T_f$  is calculated as  $\int \rho c_p (T - T_f) dx dz = 1.4 \times 10^{13}$  J m<sup>-1</sup>, where the integral is taken from 40- to 100-m depth over the full distance of the survey. Assuming a vertical heat flux of 10 W m<sup>-2</sup> from the upper edge of the CSC intrusion and that this uppermost warm layer homogenizes in six months, the total along-track heat loss is  $3 \times$

$10^{12}$  J m<sup>-1</sup>. Thus, the majority of the heat contained within the intrusion is likely sequestered in the halocline layer and not lost to vertical double-diffusive fluxes. The portion of heat which is lost vertically could be climatically relevant, as winter mixed layers can be as deep as 40 m. Heat higher than these depths is potentially available to melt sea ice if it is entrained in the mixed layer. The latent heat of sea ice ( $L_H$ ) is  $2.67 \times 10^5$  J kg<sup>-1</sup> and its density ( $\rho_{ice}$ ) is 900 kg m<sup>-3</sup>. The rate of sea ice loss can be calculated as  $F_H/L_H/\rho_{ice}$ . A vertical heat flux of 10 W m<sup>-2</sup> applied directly to sea ice would therefore correspond to a melting rate of 4 mm day<sup>-1</sup>, or 0.6 m over 6 months.

Observations from ice-tethered profiles and other distributed sampling schemes indicate that the PSW layer of the western Arctic halocline is warming, with an increase of  $\sim 1.5 \times 10^{20}$  J over the 30 years from 1987 to 2017, or  $5 \times 10^{18}$  J annually (Timmermans et al. 2018). Provided a cross-track intrusion thickness of 20 km (equivalent to the observed 20-km along-track intrusion thickness) the total heat contained in the CSC intrusion is  $3 \times 10^{17}$  J, found by multiplying by the along-track density by this 20 km thickness. This total heat content represents about 1/20th of the annual increase in PSW temperature observed by Timmermans et al. (2018). Timmermans et al. (2018) calculate the increased heat content between the 31 and 33 isohalines, so this comparison is not exact as the CSC intrusion is fresher than this range. However, at 40-m depth the intrusion is deeper than typical winter mixed layer depths in this region.

In recent years, many warm PSW flows have been observed off of Barrow Canyon and the Chukchi Slope, including multiple examples during the same process cruise in which this intrusion was surveyed (Kawaguchi et al. 2012; Timmermans and Jayne 2016; Fine et al. 2018; Boury et al. 2020; MacKinnon et al. 2021). Both the historic and modern prevalence of such features is unknown. Understanding where the heat from these features is ultimately distributed is essential to determining the heat balance of the upper halocline in the western Arctic and how this balance is changing in light of warming source waters.

**Acknowledgments.** This work was supported by ONR Grant N00014-16-1-2378 and NSF Grants PLR 14-56705 and PLR-1303791, NSF Graduate Research Fellowship Grant DGE-1650112, as well as by the Postdoctoral Scholar Program at Woods Hole Oceanographic Institution, with funding provided by the Weston Howland Jr. Postdoctoral Scholarship. We gratefully acknowledge the *Sikuliaq* captain and crew, the Modular Ocean Dynamics engineering team, and our SODA collaborators who made this study possible. We are additionally grateful to Mike Gregg, Seth Danielson, Peter Winsor, Mary-Louise Timmermans, Yueng-Djern Lenn, John Toole, and Rob Pinkel, for scientific support and insight; and to Mike Gregg, Dave Winkel, Andrew Cookson, Amy Waterhouse, and Sam Fletcher for supporting the transition of the MMP instrumentation from APL/UW to SIO. We are also thankful for insightful comments from editor Ilker Fer and from Jeff Carpenter and an anonymous reviewer, which greatly improved the manuscript.

**Data availability statement.** MODIS-Aqua SST data are provided by NASA OBPG, and are the MODIS-Aqua Global

Level 3 Mapped SST. Ver. 2019.0. PO.DAAC, CA, USA. Dataset accessed 2 February 2021 at <https://doi.org/10.5067/MODSA-8D4D9>. Microstructure data are available for download at <https://microstructure.ucsd.edu>.

## APPENDIX

### Double Diffusive Dissipation Estimation

The method described by [Middleton et al. \(2021\)](#) uses temperature and salinity data to estimate dissipation. This method relies on theoretical work by [Middleton and Taylor \(2020\)](#) linking the dissipation due to double-diffusive convection to the magnitude of gradients in the compensated thermohaline variance (“spice”). Here we provide a brief summary of the method’s assumptions and steps; for a full description and derivation please see [Middleton et al. \(2021\)](#).

The method assumes that

- turbulence occurs due to double-diffusive convection, so that the rate of dissipation of TKE is equivalent to the up-gradient diapycnal buoyancy flux ( $\langle \epsilon \rangle = -\langle \phi_d \rangle$ );
- buoyancy and spice gradients are anticorrelated; and
- submeasurement scales are dominated by quasigeostrophic stirring along isopycnals, so that spice variance scales as  $k^{-1}$  down to the Ozmidov scale at which the diapycnal flux drives convection. This scaling is taken to apply in three dimensions, with the vertical coordinate scaled by  $N/f$ .

The amplitude of the subgrid-scale spice spectra is estimated from a two-point correlation calculated locally from the observations. The resulting synthetic power spectra are then used to estimate the magnitude of the spice gradient down to the Ozmidov scale. An iterative equation is used to calculate  $\langle \epsilon \rangle$ :

$$\langle \epsilon \rangle = -\frac{\kappa_T + \kappa_S}{2b_z^*} \langle |\nabla b|^2 \rangle + g \frac{\kappa_T - \kappa_S}{2b_z^*} \langle |\nabla b| \rangle \sqrt{\frac{2}{3} + \frac{N^2}{3f^2}} \sqrt{\frac{A}{2}} k_{Oz} \quad (\text{A1})$$

in which  $\kappa_T$  and  $\kappa_S$  are the molecular diffusivities of heat and salt, respectively;  $b$  is buoyancy;  $b_z^*$  is the gradient of the sorted buoyancy profile;  $g$  is acceleration due to gravity;  $N$  is the buoyancy frequency; and  $f$  is the Coriolis frequency. Parameter  $A$  is the magnitude of the spice gradient assumed to be of the form

$$A = \frac{R(\mathbf{r})}{2 \int_0^{k_{Oz}} \tilde{k}^{-1} \left[ 1 - \cos(\tilde{r}\tilde{k}) \right] d\tilde{k}} \quad (\text{A2})$$

with  $k_{Oz}$  the wavenumber associated with the Ozmidov length scale and  $R(\mathbf{r})$  the two-point correlation of the spice field.

The algorithm to calculate  $\epsilon$  from temperature and salinity data proceeds as follows:

- 1) Calculate the two-point correlation for the spice field  $R(\mathbf{r})$

- 2) Calculate the Ozmidov scale ( $L_{Oz} = \sqrt{\epsilon/N^3}$ ) from estimated  $\langle \epsilon \rangle$ . For the first iteration a guess is used for  $\epsilon$
- 3) Calculate the amplitude of the subgrid-scale spice spectra using Eq. (A2)
- 4) Repeat steps 2–4 until  $\langle \epsilon \rangle$  converges.

## REFERENCES

- Alford, M. H., and M. C. Gregg, 2001: Near-inertial mixing: Modulation of shear, strain and microstructure at low latitude. *J. Geophys. Res.*, **106**, 16947–16968, <https://doi.org/10.1029/2000JC000370>.
- , —, and E. A. D’Asaro, 2005: Mixing, 3D mapping, and Lagrangian evolution of a thermohaline intrusion. *J. Phys. Oceanogr.*, **35**, 1689–1711, <https://doi.org/10.1175/JPO2780.1>.
- Baker, M. A., and C. H. Gibson, 1987: Sampling turbulence in the stratified ocean: Statistical consequences of strong intermittency. *J. Phys. Oceanogr.*, **17**, 1817–1836, [https://doi.org/10.1175/1520-0485\(1987\)017<1817:STITSO>2.0.CO;2](https://doi.org/10.1175/1520-0485(1987)017<1817:STITSO>2.0.CO;2).
- Bebieva, Y., and M. L. Timmermans, 2019: Double-diffusive layering in the Canada Basin: An explanation of along-layer temperature and salinity gradients. *J. Geophys. Res. Oceans*, **124**, 723–735, <https://doi.org/10.1029/2018JC014368>.
- Boury, S., and Coauthors, 2020: Whither the Chukchi slope current? *J. Phys. Oceanogr.*, **50**, 1717–1732, <https://doi.org/10.1175/JPO-D-19-0273.1>.
- Brown, J. M., and T. Radko, 2019: Initiation of diffusive layering by time-dependent shear. *J. Fluid Mech.*, **858**, 588–608, <https://doi.org/10.1017/jfm.2018.790>.
- Cole, S. T., and D. L. Rudnick, 2012: The spatial distribution and annual cycle of upper ocean thermohaline structure. *J. Geophys. Res.*, **117**, C02027, <https://doi.org/10.1029/2011JC007033>.
- Corlett, W. B., and R. S. Pickart, 2017: The Chukchi slope current. *Prog. Oceanogr.*, **153**, 50–65, <https://doi.org/10.1016/j.pcean.2017.04.005>.
- Davis, R. E., 1994: Diapycnal mixing in the ocean: The Osborn-Cox model. *J. Phys. Oceanogr.*, **24**, 2560–2576, [https://doi.org/10.1175/1520-0485\(1994\)024<2560:DMITOT>2.0.CO;2](https://doi.org/10.1175/1520-0485(1994)024<2560:DMITOT>2.0.CO;2).
- Fer, I., 2009: Weak vertical diffusion allows maintenance of cold halocline in the central Arctic. *Atmos. Ocean. Sci. Lett.*, **2**, 148–152, <https://doi.org/10.1080/16742834.2009.11446789>.
- Fine, E. C., J. A. MacKinnon, M. H. Alford, and J. B. Mickett, 2018: Microstructure observations of turbulent heat fluxes in a warm-core Canada Basin Eddy. *J. Phys. Oceanogr.*, **48**, 2397–2418, <https://doi.org/10.1175/JPO-D-18-0028.1>.
- , M. H. Alford, J. A. MacKinnon, and J. B. Mickett, 2021: Microstructure mixing observations and finescale parameterizations in the Beaufort Sea. *J. Phys. Oceanogr.*, **51**, 19–35, <https://doi.org/10.1175/JPO-D-19-0233.1>.
- Gregg, M. C., 1989: Scaling turbulent dissipation in the thermocline. *J. Geophys. Res.*, **94**, 9686, <https://doi.org/10.1029/JC094iC07p09686>.
- Guthrie, J. D., J. H. Morison, and I. Fer, 2013: Revisiting internal waves and mixing in the Arctic Ocean. *J. Geophys. Res. Oceans*, **118**, 3966–3977, <https://doi.org/10.1002/jgrc.20294>.
- Howard, L. N., 1961: Note on a paper of John W. Miles. *J. Fluid Mech.*, **10**, 509–512, <https://doi.org/10.1017/S0022112061000317>.
- Jackson, J. M., E. C. Carmack, F. A. McLaughlin, S. E. Allen, and R. G. Ingram, 2010: Identification, characterization, and change of the near-surface temperature maximum in the



- Canada Basin, 1993–2008. *J. Geophys. Res.*, **115**, C05021, <https://doi.org/10.1029/2009JC005265>.
- Kawaguchi, Y., M. Itoh, and S. Nishino, 2012: Detailed survey of a large baroclinic eddy with extremely high temperatures in the western Canada Basin. *Deep-Sea Res. I*, **66**, 90–102, <https://doi.org/10.1016/j.dsr.2012.04.006>.
- , T. Kikuchi, and R. Inoue, 2014: Vertical heat transfer based on direct microstructure measurements in the ice-free Pacific-side Arctic Ocean: The role and impact of the Pacific water intrusion. *J. Oceanogr.*, **70**, 343–353, <https://doi.org/10.1007/s10872-014-0234-8>.
- , S. Nishino, J. Inoue, K. Maeno, H. Takeda, and K. Oshima, 2016: Enhanced diapycnal mixing due to near-inertial internal waves propagating through an anticyclonic eddy in the ice-free Chukchi Plateau. *J. Phys. Oceanogr.*, **46**, 2457–2481, <https://doi.org/10.1175/JPO-D-15-0150.1>.
- Kelley, D. E., 1990: Fluxes through diffusive staircases: A new formulation. *J. Geophys. Res.*, **95**, 3365–3371, <https://doi.org/10.1029/JC095iC03p03365>.
- , H. J. Fernando, A. E. Gargett, J. Tanny, and E. Özsoy, 2003: The diffusive regime of double-diffusive convection. *Prog. Oceanogr.*, **56**, 461–481, [https://doi.org/10.1016/S0079-6611\(03\)00026-0](https://doi.org/10.1016/S0079-6611(03)00026-0).
- Klein, P., A. M. Treguier, and B. L. Hua, 1998: Three-dimensional stirring of thermohaline fronts. *J. Mar. Res.*, **56**, 589–612, <https://doi.org/10.1357/002224098765213595>.
- Lincoln, B. J., T. P. Rippeth, Y.-D. Lenn, M. L. Timmermans, W. J. Williams, and S. Bacon, 2016: Wind-driven mixing at intermediate depths in an ice-free Arctic Ocean. *Geophys. Res. Lett.*, **43**, 9749–9756, <https://doi.org/10.1002/2016GL070454>.
- MacKinnon, J. A., and Coauthors, 2021: A warm jet in a cold ocean. *Nat. Commun.*, **12**, 2418, <https://doi.org/10.1038/s41467-021-22505-5>.
- May, B. D., and D. E. Kelley, 2001: Growth and steady state stages of thermohaline intrusions in the Arctic Ocean. *J. Geophys. Res.*, **106**, 16 783–16 794, <https://doi.org/10.1029/2000JC000605>.
- Merrifield, S. T., L. S. Laurent, B. Owens, A. M. Thurnherr, and J. M. Toole, 2016: Enhanced diapycnal diffusivity in intrusive regions of the Drake Passage. *J. Phys. Oceanogr.*, **46**, 1309–1321, <https://doi.org/10.1175/JPO-D-15-0068.1>.
- Middleton, L., and J. R. Taylor, 2020: A general criterion for the release of background potential energy through double diffusion. *J. Fluid Mech.*, **893**, R3, <https://doi.org/10.1017/jfm.2020.259>.
- , E. C. Fine, J. A. MacKinnon, M. H. Alford, and J. R. Taylor, 2021: Estimating dissipation rates associated with double diffusion. *Geophys. Res. Lett.*, **48**, e2021GL092779, <https://doi.org/10.1029/2021GL092779>.
- Miles, J. W., 1961: On the stability of heterogeneous shear flows. *J. Fluid Mech.*, **10**, 496–508, <https://doi.org/10.1017/S0022112061000305>.
- Padman, L., 1994: Momentum fluxes through sheared oceanic thermohaline steps. *J. Geophys. Res.*, **99**, 22 491–22 499, <https://doi.org/10.1029/94JC01741>.
- Polzin, K. L., A. C. Naveira Garabato, T. N. Huussen, B. M. Sloyan, and S. Waterman, 2014: Finescale parameterizations of turbulent dissipation. *J. Geophys. Res. Oceans*, **119**, 1383–1419, <https://doi.org/10.1002/2013JC008979>.
- Ruddick, B. R., and J. S. Turner, 1979: The vertical length scale of double-diffusive intrusions. *Deep-Sea Res.*, **26A**, 903–913, [https://doi.org/10.1016/0198-0149\(79\)90104-3](https://doi.org/10.1016/0198-0149(79)90104-3).
- , N. S. Oakey, and D. Hebert, 2010: Measuring lateral heat flux across a thermohaline front: A model and observational test. *J. Mar. Res.*, **68**, 523–539, <https://doi.org/10.1357/002224010794657146>.
- Shibley, N. C., and M. L. Timmermans, 2019: The formation of double-diffusive layers in a weakly turbulent environment. *J. Geophys. Res. Oceans*, **124**, 1445–1458, <https://doi.org/10.1029/2018JC014625>.
- Smith, K. S., and R. Ferrari, 2009: The production and dissipation of compensated thermohaline variance by mesoscale stirring. *J. Phys. Oceanogr.*, **39**, 2477–2501, <https://doi.org/10.1175/2009JPO4103.1>.
- Sommer, T., J. R. Carpenter, and A. Wüest, 2014: Double-diffusive interfaces in Lake Kivu reproduced by direct numerical simulations. *Geophys. Res. Lett.*, **41**, 5114–5121, <https://doi.org/10.1002/2014GL060716>.
- St. Laurent, L., and R. W. Schmitt, 1999: The contribution of salt fingers to vertical mixing in the North Atlantic Tracer Release Experiment. *J. Phys. Oceanogr.*, **29**, 1404–1424, [https://doi.org/10.1175/1520-0485\(1999\)029<1404:TCOSFT>2.0.CO;2](https://doi.org/10.1175/1520-0485(1999)029<1404:TCOSFT>2.0.CO;2).
- Stroeve, J., and D. Notz, 2018: Changing state of Arctic sea ice across all seasons. *Environ. Res. Lett.*, **13**, 103001, <https://doi.org/10.1088/1748-9326/aaade56>.
- Timmermans, M.-L., and P. Winsor, 2013: Scales of horizontal density structure in the Chukchi Sea surface layer. *Cont. Shelf Res.*, **52**, 39–45, <https://doi.org/10.1016/j.csr.2012.10.015>.
- , and S. R. Jayne, 2016: The Arctic Ocean spices up. *J. Phys. Oceanogr.*, **46**, 1277–1284, <https://doi.org/10.1175/JPO-D-16-0027.1>.
- , S. Cole, and J. Toole, 2012: Horizontal density structure and restratification of the Arctic Ocean surface layer. *J. Phys. Oceanogr.*, **42**, 659–668, <https://doi.org/10.1175/JPO-D-11-0125.1>.
- , and Coauthors, 2014: Mechanisms of Pacific summer water variability in the Arctic's central Canada Basin. *J. Geophys. Res. Oceans*, **119**, 7523–7548, <https://doi.org/10.1002/2014JC010273>.
- , J. Toole, and R. Krishfield, 2018: Warming of the interior Arctic Ocean linked to sea ice losses at the basin margins. *Sci. Adv.*, **4**, eaat6773, <https://doi.org/10.1126/sciadv.aat6773>.
- Toole, J. M., M. L. Timmermans, D. K. Perovich, R. A. Krishfield, A. Proshutinsky, and J. A. Richter-Menge, 2010: Influences of the ocean surface mixed layer and thermohaline stratification on Arctic Sea ice in the central Canada Basin. *J. Geophys. Res.*, **115**, C10018, <https://doi.org/10.1029/2009JC005660>.
- Umlauf, L., P. L. Holtermann, C. A. Gillner, R. D. Prien, L. Merckelbach, and J. R. Carpenter, 2018: Diffusive convection under rapidly varying conditions. *J. Phys. Oceanogr.*, **48**, 1731–1747, <https://doi.org/10.1175/JPO-D-18-0018.1>.
- Veronis, G., 1972: On properties of seawater defined by temperature, salinity, and pressure. *J. Mar. Res.*, **30**, 227–255.
- Werdell, P. J., and Coauthors, 2013: Generalized ocean color inversion model for retrieving marine inherent optical properties. *Appl. Opt.*, **52**, 2019–2037, <https://doi.org/10.1364/AO.52.002019>.
- Whalen, C. B., J. A. MacKinnon, L. D. Talley, and A. F. Waterhouse, 2015: Estimating the mean diapycnal mixing using a finescale strain parameterization. *J. Phys. Oceanogr.*, **45**, 1174–1188, <https://doi.org/10.1175/JPO-D-14-0167.1>.
- Woodgate, R. A., 2018: Increases in the Pacific inflow to the Arctic from 1990 to 2015, and insights into seasonal trends and driving mechanisms from year-round Bering Strait mooring data. *Prog. Oceanogr.*, **160**, 124–154, <https://doi.org/10.1016/j.pcean.2017.12.007>.